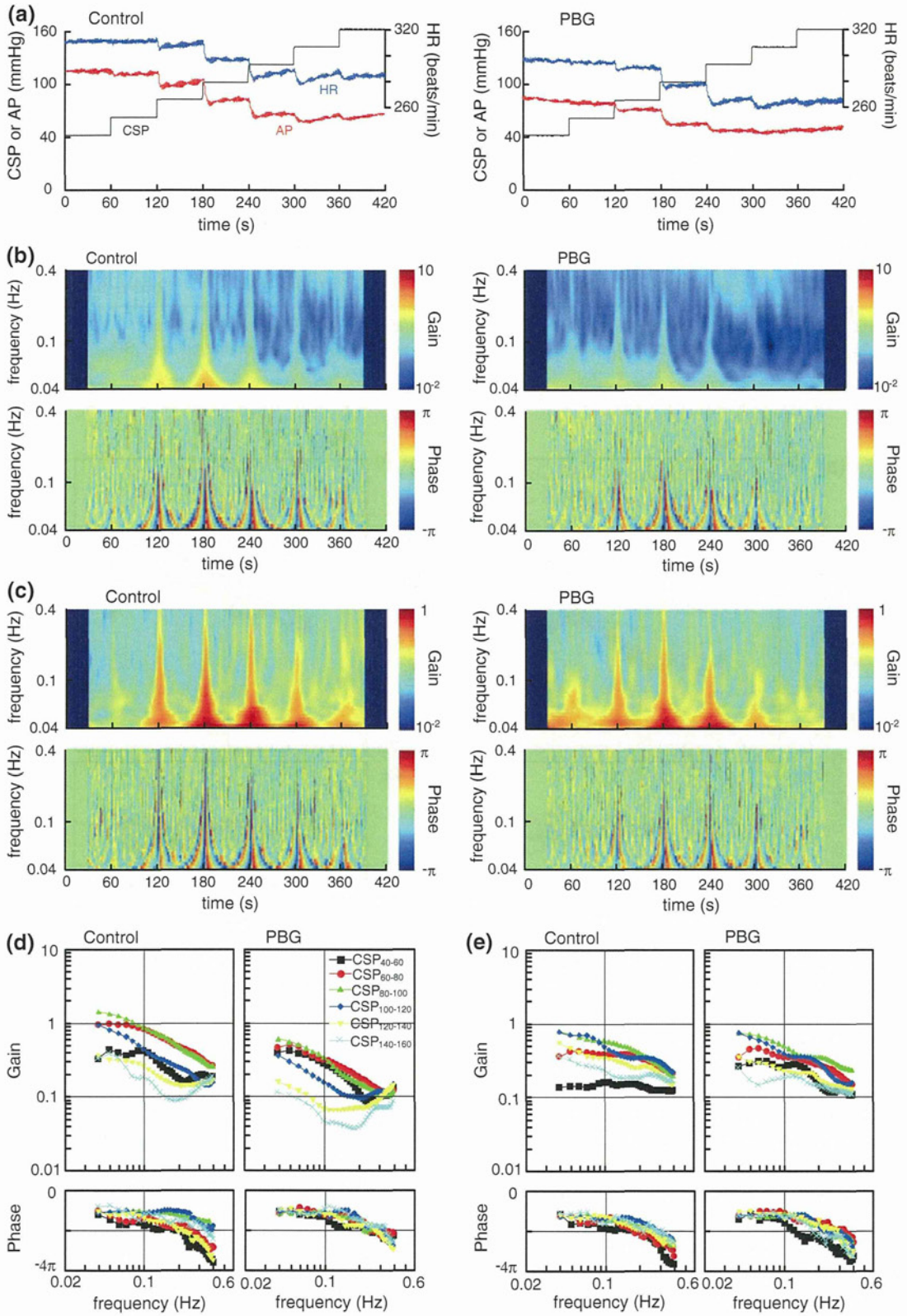

FIGURE 6. (a) Averaged (n = 8) time series of CSP, AP, and HR obtained in the absence (Control, *left*) and presence of phenylbiguanide (PBG, *right*). CSP was increased from 40 to 160 mmHg in 20 mmHg increments, resulting in changes in AP and HR through the carotid sinus baroreflex. Time-series transfer functions of total loop (b) and cardiac baroreflex (c) in the Control (*left*) and PBG (*right*) conditions. Average (n = 8) gain (*top*) and phase (*bottom*). Transfer functions of total loop (d) and cardiac baroreflex (e) estimated by wavelet analysis in the Control (*left*) and PBG (*right*) conditions.

TABLE 2. Parameters of the transfer functions for the total loop and cardiac baroreflex before and during PBG infusion.

	Low CSP (40–60 mmHg)		Middle CSP (80–100 mmHg)		High CSP (120–140 mmHg)	
	Control	PBG	Control	PBG	Control	PBG
Total loop						
$G_{0.04}$	0.32 ± 0.07	0.39 ± 0.09††	1.39 ± 0.15	0.59 ± 0.09**,††	0.35 ± 0.04††	0.15 ± 0.02††
Slope (dB/decade)	−11.6 ± 3.3	−8.0 ± 4.2	−17.8 ± 2.1	−15.0 ± 3.2	−6.5 ± 2.5	7.4 ± 5.3††
Lag time (s)	2.90 ± 0.71	1.43 ± 0.68	1.44 ± 0.22	2.21 ± 0.59	3.48 ± 0.61	2.74 ± 0.89
Cardiac baroreflex						
$G_{0.04}$ (beats/min/mmHg)	0.14 ± 0.02	0.26 ± 0.10†	0.78 ± 0.21	0.75 ± 0.18	0.54 ± 0.13	0.35 ± 0.08†
Slope (dB/decade)	−1.8 ± 2.2	−12.5 ± 2.9*	−13.4 ± 2.7	−11.6 ± 2.1	−12.6 ± 2.7	−6.6 ± 4.0
Lag time (s)	2.99 ± 0.89	2.91 ± 0.55	2.06 ± 0.30	2.28 ± 0.54	2.65 ± 0.72	2.47 ± 0.77

$G_{0.04}$, transfer gain at 0.04 Hz. Slope, average slope of gain between 0.1 and 0.4 Hz. PBG, phenylbiguanide.
** $p < 0.01$ and * $p < 0.05$, PBG vs. Control at the same CSP; †† $p < 0.01$ and † $p < 0.05$, all conditions vs. CSP_{80-100} of Control.

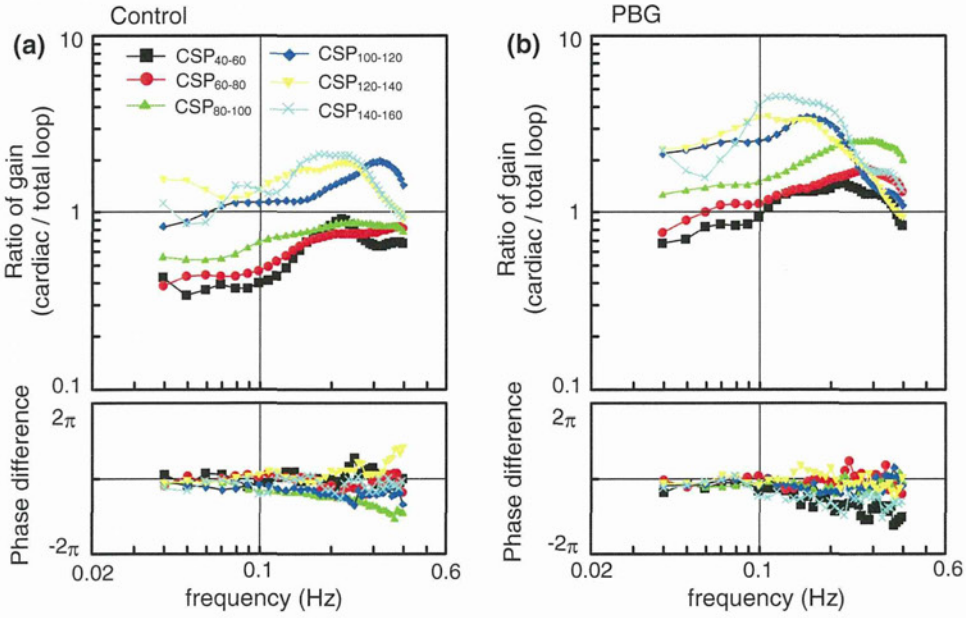

FIGURE 7. The ratio in the transfer functions of the cardiac baroreflex (CSP-HR) to the total loop (CSP-AP) (n = 8). The ratio of dynamic gain (*top*) and the phase difference (*bottom*). Control (a) and PBG (b) conditions.

transform that can adjust the analysis window at every frequency level and extract the localized data. When the mother wavelet is appropriately used for any purpose, the fields of the application of wavelet analysis might be extended. We used the traditional and reasonable Morlet function;[11,48,49] however, the comparison with other wavelet functions such as Mexican hat, Haar, and Daubechies[34] will be required in future studies. In addition, the convolutions within the transfer function of Eq. (3) may lose the temporal information; however, because the wavelet transform reflects the effect of reasonably changed time window, the gain and phase updated every 0.2 s can continuously express the representative property at the center point of the time window during the time-course change.

Physiological Perspective

The powers of the RSNA, AP, and HR responses to CSP changes showed maximum values at CSP_{80-100} change (Fig. 3b), which was almost consistent with AP_{OP} (94.3 and 99.7 mmHg) from static analysis. In contrast, the power responses at CSP_{40-60} and $CSP_{140-160}$ changes were lower than those at AP_{OP}, resulting from the nonlinear characteristics of the baroreflex around threshold and saturation to AP inputs as indicated by the static analysis. The gain and phase were revealed within the physiological range including nonlinear points in normal rabbits (Figs. 4 and 5). Whereas the static analysis cannot show the dynamic characteristics at higher frequencies (e.g. >0.01 Hz[18]), the proposed wavelet-based analysis

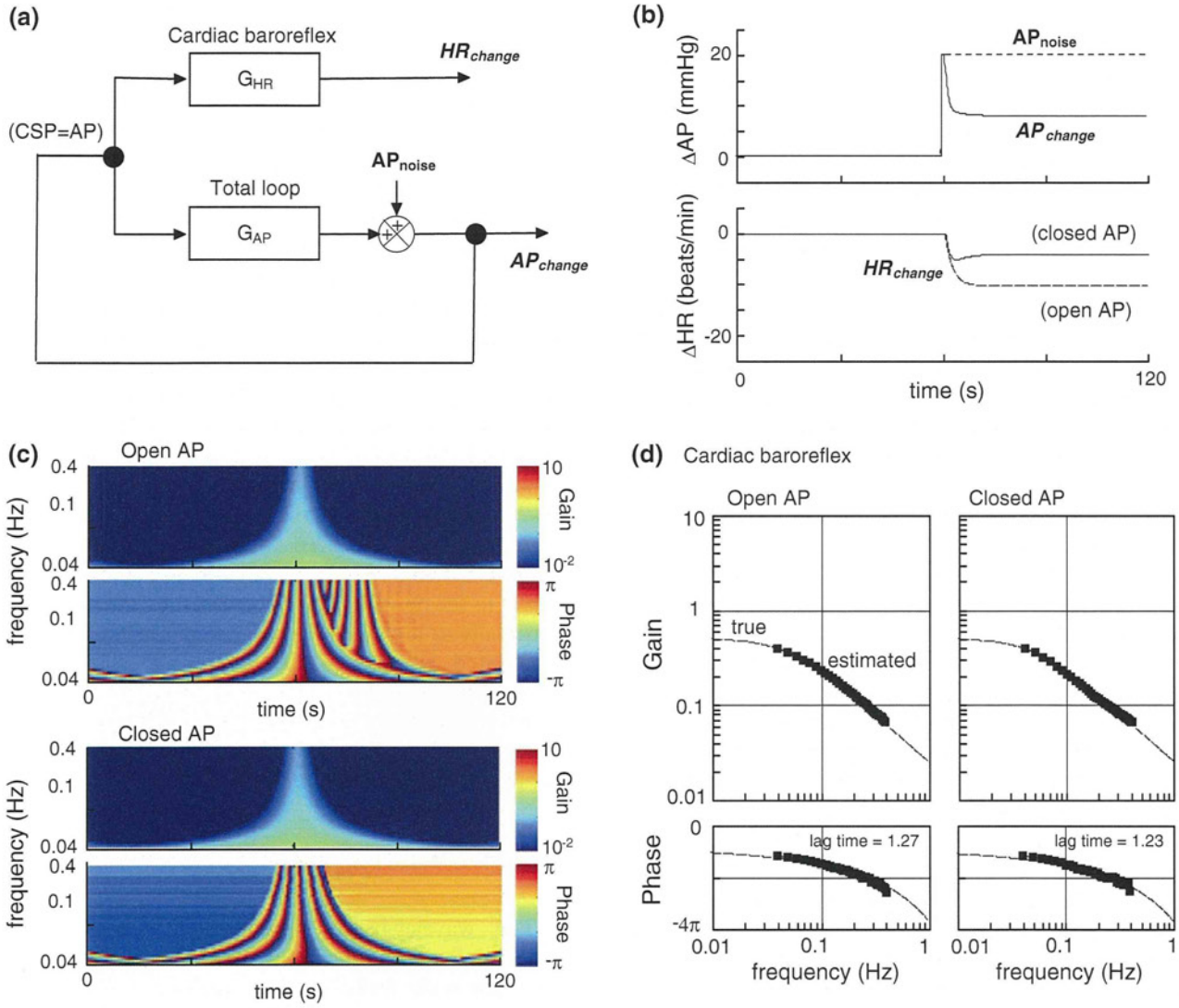

FIGURE 8. (a) Block diagram of cardiac baroreflex under closed-loop AP response. AP_{noise} indicates the external disturbance to AP. AP_{change} and HR_{change} show the actual changes of AP and HR. G_{AP} and G_{HR} are transfer functions under open loop responses in the total loop and cardiac baroreflex. (b) AP_{noise} of +20 mmHg as input and AP_{change} as output under the closed loop (*top*). HR responses under the open- and closed-loop AP changes (*bottom*). (c) Time-series transfer functions of cardiac baroreflex under open- and closed-loop AP changes. (d) Transfer functions of cardiac baroreflex estimated under the open (*left*) and closed (*right*) AP responses. Gain (*top*) and phase (*bottom*). Dotted lines, theoretical values. Squares, estimated values by our wavelet analysis.

could derive them from the same step input protocol, which may be able to reduce the number of experiments and duration of data acquisition.

Clinical Implications for Cardiac Patients

The wavelet-based system identification indicated a possibility to acquire pathophysiological understanding under various responses with cardiac diseases. The proposed analysis revealed that the dynamic characteristics in the total loop and neural arc were significantly attenuated at various pressure changes containing nonlinear points under PBG condition (Fig. 6 and Table 2), in addition to the previous studies.[18,20] The $G_{0.04}$ at AP_{OP} in Control (1.39 ± 0.15) was decreased to almost half during PBG condition (0.59 ± 0.09); it was attenuated to 1/3–1/4 times as small as that under PBG condition (0.39 ± 0.09) at low CSP_{40-60} change, which may be induced by the decrease of peripheral pump function in heart failure, suggesting the risk of further bluntness of baroreflex ability during the BJR.

In carotid-cardiac response, HR may be related to the assessment of AP regulation by the product of HR, stroke volume, and total peripheral resistance, rather than RR interval.[7,8] Because it may be difficult to evaluate the baroreflex to regulate AP under the carotid-sinus closed loop condition (i.e. CSP = AP), we

explored the possibility to evaluate the baroreflex dynamics from the HR response related to AP regulation, considering the dissociation between animal and human studies and applying the proposed method. The transfer functions of the cardiac baroreflex were similar to those of the total loop around the operating point (Fig. 7a). On the other hand, the dynamic characteristics in nonlinear CSP points and during the BJR were greater than those around the operating point in Control condition (Fig. 7b), suggesting the effect of cardiac sympathovagal activity. Next, to consider human baroreflex assessment, the dynamic transfer function was estimated by the closed-loop model response (Fig. 8), resulting in the effective assessment. Even when the system input is modulated by the nature of closed-loop response, it would be crucial to be able to estimate the dynamic baroreflex characteristics.

The spontaneous baroreflex method is commonly used in clinical assessments.[37] This method may have some limitations because of the highly complex and interconnected cardiovascular mechanisms in short-term AP regulation[27,40,43] and the unclear system input might induce the different pathophysiological understandings.[42] On the other hand, our focus was to explore the possibility of the evaluation of the baroreflex to regulate AP against great external disturbances in patients with cardiovascular diseases and unstable hemodynamics. To identify the system dynamics of the carotid-sinus baroreflex for AP regulation with sympathovagal activity,[51] this study improved the standard analyses, particularly considering the pure time delay. Using the transfer function corresponding to the independent step input frequency, the proposed analysis was able to indicate some novel aspects of the dynamic baroreflex properties during the BJR as mentioned above.

For clinical application, the other indexes (e.g. AP to muscle SNA response[14]) for AP regulation might be tested. In addition, in the time-course data, there are some effective methods such as complex demodulation method[13] based on the low pass filter, focusing on a frequency band such as LF and HF; it has good temporal resolution. However, the complex demodulation method might concentrate on the information of amplitude in a frequency band, not on each frequency level within the band. This limitation makes it impossible to perform the system identification in this study to reproduce the response corresponding to a wide frequency. Furthermore, the continuous estimation of the dynamics might connect to an effective index of the real-time control of hemodynamics such as an automated drug infusion system.[17,19]

Because we kept the bilateral vagi intact, low pressure baroreflexes from the cardiopulmonary region might have interacted with the arterial baroreflex, affecting estimation of carotid sinus baroreflex transfer functions. After the vagotomy, the dynamics from isolated aortic depressor nerve to AP responses was almost preserved and AP remained unchanged despite a HR decrease.[28,46] Our previous data of dynamic baroreflex properties with[20] and without[21] vagal nerves were compared. The dynamic characteristics of the total loop and cardiac baroreflex around the operating point were similar, whereas the corner frequency was slightly greater under intact vagal condition. Next, the static gain may be increased during the rising pressure protocol, compared with the falling one.[46] Hysteresis induced by the rising and falling pressure protocols may also modulate the dynamic baroreflex. However, the vagal effect of the cardiovascular receptors on the dynamics may not be large.[28] Third, the phases at lower or higher CSP changes in the transfer functions varied with the observed frequency because of nonlinear characteristics in the neural arc and the input power in the peripheral arc decreased by the neural arc. Especially at high frequencies, the phases appear to be modulated because of the step input showing low power with the high frequency. Finally, the simple models used for the simulations in this study have some limitations, such as a lack of information of nonparametric components or nonlinearity.[23]

CONCLUSIONS

The wavelet-based time-frequency analysis was capable of identifying the dynamic baroreflex properties over wide frequencies at various pressure levels both in normal and BJR conditions. Because the dynamic baroreflex properties to physiological pressure inputs as well as static characteristics can be simultaneously extracted from the short-term responses with background noise, the proposed method is potentially applicable to assess human dynamic baroreflex function under carotid-sinus closed-loop condition.

APPENDIX

Model Response of Arterial Baroreflex

We used the following model[15] as the carotid sinus open loop baroreflex for the simulation study (Figs. 1 and 2). The neural arc transfer function [$G_N(f)$] using a first-order high-pass filter can be expressed as

$$G_N(f) = -K_N\left(1 + \frac{f}{f_C}i\right)\exp(-2\pi f i L_N)$$

where f and i represent the frequency (Hz) and imaginary units, respectively; K_N is the neural arc gain; f_C is the frequency (Hz) for a derivative characteristic; L_N is lag time (s).

The peripheral arc transfer function [$G_P(f)$] using a second-order low-pass filter can be expressed as

$$G_P(f) = \frac{K_P}{1 + 2\zeta\frac{f}{f_N}i + \left(\frac{f}{f_N}i\right)^2} \exp(-2\pi f i L_P)$$

where K_P, f_N, ζ, and L_P represent the peripheral arc gain, natural frequency (Hz), damping ratio, and lag time (s), respectively.

The transfer function of the total baroreflex loop is expressed as the product of the neural and peripheral arc transfer functions.

$$G_{AP}(f) = G_N(f) \cdot G_P(f)$$

The gain and lag time of the total baroreflex loop is expressed as $K = K_N \cdot K_P$ and $L = L_N + L_P$. The parameters of the model response were set at $K = 1.0$, $f_C = 0.12$, $L_N = 0.55$, $f_N = 0.071$, $\zeta = 1.37$, and $L_P = 1.0$ according to previous data.[15]

Model of Baroreflex Under Closed-Loop AP Response

The baroreflex system under the closed-loop AP input to HR response was modeled (Fig. 8a).

$$HR_{change}(f) = G_{HR}(f) \cdot AP_{change}(f)$$

The pressure change [$AP_{change}(f)$] to the exogenous perturbation [$AP_{noise}(f)$] is the sum of the feedback signal and perturbation under closed-loop condition.[15] G_{HR} is the transfer function under the carotid sinus open loop in the cardiac baroreflex (CSP input and HR output).

$$AP_{change}(f) = G_{AP}(f) \cdot AP_{change}(f) + AP_{noise}(f)$$

Rearranging above equation with respect to $AP_{change}(f)$ yields

$$AP_{change}(f) = \frac{AP_{noise}(f)}{1 - G_{AP}(f)}$$

The time integral of the inverse Fourier transform of $AP_{change}(f)$ is the AP change to an exogenous step perturbation. G_{AP} is the transfer function under the carotid sinus open loop for the total baroreflex. The AP_{change} and HR_{change} can be simply observed by the monitoring system. The transfer function between the HR and AP responses was excluded because of the insignificant relationship as previously indicated.[22]

The transfer functions, G_{AP} and G_{HR}, were approximated using a first-order low-pass filter.

$$G(f) = \frac{-K}{\left(1 + \frac{f}{f_C}i\right)} \cdot \exp(-2\pi f i L)$$

The parameters of the transfer functions were set at $K = 1.03$, $f_C = 0.018$, and $L = 1.34$ for the total loop (Fig. 8a, G_{AP}); $K = 0.51$, $f_C = 0.049$, and $L = 1.14$ for the cardiac baroreflex (G_{HR}), according to previous data.[20]

ACKNOWLEDGMENTS

This study was supported by "Health and Labour Sciences Research Grant for Research on Advanced Medical Technology", "Health and Labour Sciences Research Grant for Research on Medical Devices for Analyzing, Supporting and Substituting the Function of Human Body", "Health and Labour Sciences Research Grant H18-Iryo-Ippan-023" from the Ministry of Health, Labour and Welfare of Japan, "Program for Promotion of Fundamental Studies in Health Science" from the National Institute of Biomedical Innovation, and "a Grant-in-Aid for Young Scientists (B)" from the Ministry of Education, Culture, Sports, Science and Technology of Japan (KAKENHI, 20700392).

REFERENCES

[1]Ando, S., H. R. Dajani, B. L. Senn, G. E. Newton, and J. S. Floras. Sympathetic alternans. Evidence for arterial baroreflex control of muscle sympathetic nerve activity in congestive heart failure. *Circulation* 95:316–319, 1997.

[2]Burgess, D. E., D. C. Randall, R. O. Speakman, and D. R. Brown. Coupling of sympathetic nerve traffic and BP at very low frequencies is mediated by large-amplitude events. *Am. J. Physiol. Regul. Integr. Comp. Physiol.* 284:R802–R810, 2003.

[3]Dampney, R. A. Functional organization of central pathways regulating the cardiovascular system. *Physiol. Rev.* 74:323–364, 1994.

[4]Davrath, L. R., Y. Goren, I. Pinhas, E. Toledo, and S. Akselrod. Early autonomic malfunction in normotensive individuals with a genetic predisposition to essential hypertension. *Am. J. Physiol. Heart Circ. Physiol.* 285:H1697–H1704, 2003.

[5]Eckberg, D. L., and T. A. Kuusela. Human vagal baroreflex sensitivity fluctuates widely and rhythmically at very low frequencies. *J. Physiol.* 567:1011–1019, 2005. doi:10.1113/jphysiol.2005.091090.

[6]Ellenbogen, K. A., P. K. Mohanty, S. Szentpetery, and M. D. Thames. Arterial baroreflex abnormalities in heart failure: reversal after orthotopic cardiac transplantation. *Circulation* 79:51–58, 1989.

[7]Fadel, P. J., S. Ogoh, D. M. Keller, and P. B. Raven. Recent insights into carotid baroreflex function in humans

using the variable pressure neck chamber. *Exp. Physiol.* 88:671–680, 2003. doi:10.1113/eph8802650.

[8]Fadel, P. J., M. Stromstad, D. W. Wray, S. A. Smith, P. B. Raven, and N. H. Secher. New insights into differential baroreflex control of heart rate in humans. *Am. J. Physiol. Heart Circ. Physiol.* 284:H735–H743, 2003.

[9]Glantz, S. A. Primer of Biostatistics. 4th ed. New York: McGraw Hill, 1997.

[10]Grassi, G., C. Turri, G. Seravalle, G. Bertinieri, A. Pierini, and G. Mancia. Effects of chronic clonidine administration on sympathetic nerve traffic and baroreflex function in heart failure. *Hypertension* 38:286–291, 2001. doi:10.1161/hy1201.096117.

[11]Grossmann, A., R. Kronland-Martinet, and J. Morlet. Reading and understanding continuous wavelets transforms. In: Wavelets, Time-Frequency Methods and Phase Space, edited by J. M. Combes, A. Grossmann, and P. Tchamitchian. Berlin: Springer, 1989, pp. 2–20.

[12]Guyton, A. C., T. G. Coleman, and H. J. Granger. Circulation: overall regulation. *Annu. Rev. Physiol.* 34:13–46, 1972. doi:10.1146/annurev.ph.34.030172.000305.

[13]Hayano, J., J. A. Taylor, S. Mukai, A. Okada, Y. Watanabe, K. Takata, and T. Fujinami. Assessment of frequency shifts in R-R interval variability and respiration with complex demodulation. *J. Appl. Physiol.* 77:2879–2888, 1994.

[14]Ichinose, M., M. Saito, N. Kondo, and T. Nishiyasu. Time-dependent modulation of arterial baroreflex control of muscle sympathetic nerve activity during isometric exercise in humans. *Am. J. Physiol. Heart Circ. Physiol.* 290:H1419–H1426, 2006. doi:10.1152/ajpheart.00847.2005.

[15]Ikeda, Y., T. Kawada, M. Sugimachi, O. Kawaguchi, T. Shishido, T. Sato, H. Miyano, W. Matsuura, J. Alexander, Jr., and K. Sunagawa. Neural arc of baroreflex optimizes dynamic pressure regulation in achieving both stability and quickness. *Am. J. Physiol. Heart Circ. Physiol.* 271:H882–H890, 1996.

[16]Jordan, J., H. R. Toka, K. Heusser, O. Toka, J. R. Shannon, J. Tank, A. Diedrich, C. Stabroth, M. Stoffels, R. Naraghi, W. Oelkers, H. Schuster, H. P. Schobel, H. Haller, and F. C. Luft. Severely impaired baroreflex-buffering in patients with monogenic hypertension and neurovascular contact. *Circulation* 102:2611–2618, 2000.

[17]Kashihara, K. Automatic regulation of hemodynamic variables in acute heart failure by a multiple adaptive predictive controller based on neural networks. *Ann. Biomed. Eng.* 34:1846–1869, 2006. doi:10.1007/s10439-006-9190-9.

[18]Kashihara, K., T. Kawada, M. Li, M. Sugimachi, and K. Sunagawa. Bezold-Jarisch reflex induced by phenylbiguanide lowers arterial pressure mainly via the downward shift of the baroreflex neural arc. *Jpn. J. Physiol.* 54:395–404, 2004. doi:10.2170/jjphysiol.54.395.

[19]Kashihara, K., T. Kawada, K. Uemura, M. Sugimachi, and K. Sunagawa. Adaptive predictive control of arterial blood pressure based on a neural network during acute hypotension. *Ann. Biomed. Eng.* 32:1365–1383, 2004. doi:10.1114/B:ABME.0000042225.19806.34.

[20]Kashihara, K., T. Kawada, Y. Yanagiya, K. Uemura, M. Inagaki, H. Takaki, M. Sugimachi, and K. Sunagawa. Bezold-Jarisch reflex attenuates dynamic gain of baroreflex neural arc. *Am. J. Physiol. Heart Circ. Physiol.* 285:H833–H840, 2003.

[21]Kashihara, K., Y. Takahashi, K. Chatani, T. Kawada, C. Zheng, M. Li, M. Sugimachi, and K. Sunagawa. Intravenous angiotensin II does not affect dynamic baroreflex characteristics of the neural or peripheral arc. *Jpn. J. Physiol.* 53:135–143, 2003. doi:10.2170/jjphysiol.53.135.

[22]Kawada, T., T. Miyamoto, K. Uemura, K. Kashihara, A. Kamiya, M. Sugimachi, and K. Sunagawa. Effects of neuronal norepinephrine uptake blockade on baroreflex neural and peripheral arc transfer characteristics. *Am. J. Physiol. Regul. Integr. Comp. Physiol.* 286:R1110–1120, 2004. doi:10.1152/ajpregu.00527.2003.

[23]Kawada, T., Y. Yanagiya, K. Uemura, T. Miyamoto, C. Zheng, M. Li, M. Sugimachi, and K. Sunagawa. Input-size dependence of the baroreflex neural arc transfer characteristics. *Am. J. Physiol. Heart Circ. Physiol.* 284:H404–H415, 2003.

[24]Kent, B. B., J. W. Drane, B. Blumenstein, and J. W. Manning. A mathematical model to assess changes in the baroreceptor reflex. *Cardiology* 57:295–310, 1972.

[25]Landesberg, G., D. Adam, Y. Berlatzky, and S. Akselrod. Step baroreflex response in awake patients undergoing carotid surgery: time- and frequency-domain analysis. *Am. J. Physiol.* 274:H1590–H1597, 1998.

[26]Lee, D. Coherent oscillations in neuronal activity of the supplementary motor area during a visuomotor task. *J. Neurosci.* 23:6798–6809, 2003.

[27]Lipman, R. D., J. K. Salisbury, and J. A. Taylor. Spontaneous indices are inconsistent with arterial baroreflex gain. *Hypertension* 42:481–487, 2003. doi:10.1161/01.HYP.0000091370.83602.E6.

[28]Liu, H. K., S. J. Guild, J. V. Ringwood, C. J. Barrett, B. L. Leonard, S. K. Nguang, M. A. Navakatikyan, and S. C. Malpas. Dynamic baroreflex control of blood pressure: influence of the heart vs. peripheral resistance. *Am. J. Physiol. Regul. Integr. Comp. Physiol.* 283:R533–R542, 2002.

[29]Lucini, D., M. Pagani, G. S. Mela, and A. Malliani. Sympathetic restraint of baroreflex control of heart period in normotensive and hypertensive subjects. *Clin. Sci. (Lond.)* 86:547–556, 1994.

[30]Malliani, A., M. Pagani, F. Lombardi, and S. Cerutti. Cardiovascular neural regulation explored in the frequency domain. *Circulation* 84:482–492, 1991.

[31]Marmarelis, P. Z., and V. Z. Marmarelis. The white noise method in system identification. In: Analysis of Physiological Systems. New York: Plenum, 1978, pp. 131–221.

[32]Masaki, H., T. Imaizumi, Y. Harasawa, and A. Takeshita. Dynamic arterial baroreflex in rabbits with heart failure induced by rapid pacing. *Am. J. Physiol.* 267:H92–H99, 1994.

[33]Mohrman, D. E., and L. J. Heller. Cardiovascular Physiology. 4th ed. New York: McGraw-Hill, 1997.

[34]Motard, R. L., and B. Joseph. Wavelet Applications in Chemical Engineering. Boston: Kluwer Academic Publishers, 1994.

[35]Munakata, M., Y. Imai, H. Takagi, M. Nakao, M. Yamamoto, and K. Abe. Altered frequency-dependent characteristics of the cardiac baroreflex in essential hypertension. *J. Auton. Nerv. Syst.* 49:33–45, 1994. doi:10.1016/0165-1838(94)90018-3.

[36]Osculati, G., G. Grassi, C. Giannattasio, G. Seravalle, F. Valagussa, A. Zanchetti, and G. Mancia. Early alterations of the baroreceptor control of heart rate in patients with acute myocardial infarction. *Circulation* 81:939–948, 1990.

[37]Parati, G., M. DiRienzo, and G. Mancia. Dynamic modulation of baroreflex sensitivity in health and disease. *Ann. NY Acad. Sci.* 940:469–487, 2001.

[38]Parati, G., J. P. Saul, and P. Castiglioni. Assessing arterial baroreflex control of heart rate: new perspectives. *J. Hypertens.* 22:1259–1263, 2004. doi:10.1097/01.hjh.0000125469.35523.32.

[39]Parmer, R. J., J. H. Cervenka, and R. A. Stone. Baroreflex sensitivity and heredity in essential hypertension. *Circulation* 85:497–503, 1992.

[40]Persson, P. B., M. DiRienzo, P. Castiglioni, C. Cerutti, M. Pagani, N. Honzikova, S. Akselrod, and G. Parati. Time versus frequency domain techniques for assessing baroreflex sensitivity. *J. Hypertens.* 19:1699–1705, 2001. doi:10.1097/00004872-200110000-00001.

[41]Pinna, G. D., R. Maestri, G. Raczak, and M. T. La Rovere. Measuring baroreflex sensitivity from the gain function between arterial pressure and heart period. *Clin. Sci. (Lond.)* 103:81–88, 2002.

[42]Pitzalis, M. V., F. Mastropasqua, A. Passantino, F. Massari, L. Ligurgo, C. Forleo, C. Balducci, F. Lombardi, and P. Rizzon. Comparison between noninvasive indices of baroreceptor sensitivity and the phenylephrine method in post-myocardial infarction patients. *Circulation* 97:1362–1367, 1998.

[43]Porta, A., G. Baselli, O. Rimoldi, A. Malliani, and M. Pagani. Assessing baroreflex gain from spontaneous variability in conscious dogs: role of causality and respiration. *Am. J. Physiol. Heart Circ. Physiol.* 279:H2558–H2567, 2000.

[44]Radaelli, A., L. Bernardi, F. Valle, S. Leuzzi, F. Salvucci, L. Pedrotti, E. Marchesi, G. Finardi, and P. Sleight. Cardiovascular autonomic modulation in essential hypertension. Effect of tilting. *Hypertension* 24:556–563, 1994.

[45]Rudas, L., A. A. Crossman, C. A. Morillo, J. R. Halliwill, K. U. Tahvanainen, T. A. Kuusela, and D. L. Eckberg. Human sympathetic and vagal baroreflex responses to sequential nitroprusside and phenylephrine. *Am. J. Physiol.* 276:H1691–H1698, 1999.

[46]Sagawa, K. Baroreflex control of systemic arterial pressure and vascular bed. In: Handbook of Physiology. The Cardiovascular System. Peripheral Circulation and Organ Blood Flow, sect. 2, vol. III, pt. 2, chap. 14. Bethesda, MD: Am. Physiol. Soc., 1983, pp. 453–496.

[47]Sato, T., T. Kawada, M. Inagaki, T. Shishido, H. Takaki, M. Sugimachi, and K. Sunagawa. New analytic framework for understanding sympathetic baroreflex control of arterial pressure. *Am. J. Physiol.* 276:H2251–H2261, 1999.

[48]Sinkkonen, J., H. Tiitinen, and R. Naatanen. Gabor filters: an informative way for analysing event-related brain activity. *J. Neurosci. Methods* 56:99–104, 1995. doi:10.1016/0165-0270(94)00111-S.

[49]Tallon-Baudry, C., O. Bertrand, C. Delpuech, and J. Pernier. Stimulus specificity of phase-locked and non-phase-locked 40 Hz visual responses in human. *J. Neurosci.* 16:4240–4249, 1996.

[50]Toledo, E., O. Gurevitz, H. Hod, M. Eldar, and S. Akselrod. Wavelet analysis of instantaneous heart rate: a study of autonomic control during thrombolysis. *Am. J. Physiol. Regul. Integr. Comp. Physiol.* 284:R1079–R1091, 2003.

[51]Westerhof, B. E., J. Gisolf, J. M. Karemaker, K. H. Wesseling, N. H. Secher, and J. J. van Lieshout. Time course analysis of baroreflex sensitivity during postural stress. *Am. J. Physiol. Heart Circ. Physiol.* 291:H2864–H2874, 2006. doi:10.1152/ajpheart.01024.2005.

[52]Zhang, R., K. Behbehani, C. G. Crandall, J. H. Zuckerman, and B. D. Levine. Dynamic regulation of heart rate during acute hypotension: new insight into baroreflex function. *Am. J. Physiol. Heart Circ. Physiol.* 280:H407–H419, 2001.

Journal of Computational Science and Technology

Vol.3, No.1, 2009

Study on Compressibility Control of Hyperelastic Material for Homogenization Method Using Mixed Finite Element Analysis*

Jun-ichi OKADA** and Toshiaki HISADA***

** Graduate School of Frontier Sciences, University of Tokyo,
5-1-5 Kashiwanoha, Kashiwa, Chiba 277-8563, Japan
E-mail: okada@sml.k.u-tokyo.ac.jp

*** Graduate School of Frontier Sciences, University of Tokyo,
7-3-1 Hongo, Bunkyo-ku, Tokyo, 113-0031, Japan
E-mail: hisada@mech.t.u-tokyo.ac.jp

Abstract

It is well known that the compressibility or incompressibility of biological tissue stems from its microscopic structure, which is generally composed of material with varied compressibility, including incompressibility. This paper proposes a framework for a homogenization method in which the compressibility/incompressibility of the macrostructure properly reflects that of the microstructure. The formulation is based on the mixed variational principle with a perturbed Lagrange-multiplier. It is shown that the rate of volumetric change of the macrostructure can be controlled through the homogenization procedure by introducing the constraint on the microstructure only. A couple of numerical examples are given to demonstrate the validity of the proposed method. By comparing the numerical results with theoretical solutions, the method is also confirmed to be free from locking.

Key words : Homogenization Method, Mixed Finite Element Analysis, Incompressible Materials, Compressible Materials, Hyper-Elasticity, Heart

1. Introduction

The homogenization method is a mathematical modeling technique for efficiently analyzing inhomogeneous material with a periodic microstructure. To measure the change in the spatial domain, we introduce two scales, namely, a scale for the microunit, and a scale for the whole material. By solving the governing equations of both scales with coupling, we can obtain the macroscopic characteristic as an equivalent homogeneous body and variable distribution in the microstructure. To investigate the effect of intracellular structure on heartbeat, we are developing the necessary finite element method in which the heart is analyzed as the macrostructure, and the cardiomyocyte as the microstructure.

In biomaterial, the periodicity hypothesized in the homogenization method is not strictly established. However, Terada et al.[1] have shown that an appropriate equivalent characteristic is obtained in material with an irregular microstructure, if the periodic boundary condition is applied. Thus it is possible to evaluate the effect of each component in the microstructure on the macroscopic behavior, if the microstructure modeling is appropriate. The homogenization method for biomaterial has been applied to bone by Hollister et al.[2], while a two-dimensional analysis of engineered tissue cells has been conducted by Breuls et al.[3]. In an example using the heart, Wanda et al.[4] have applied an excitation propagation phenomena.

Biomaterial is usually modeled by hyperelastic material. However, the myofibril in the cardiomyocyte generates contraction forces and stiffness changed by chemical reaction and includes anisotropic high nonlinearity. In addition, the organization of cytoplasm, mitochondria, nucleus, microtubule, and so on are different intra-cellularly and these also have different

*Received 20 Nov., 2008 (No.T1-07-0579)
Japanese Original: Trans. Jpn. Soc. Mech. Eng., Vol.73, No.735, A (2007), pp.1201–1208 (Received 20 June, 2007)
[DOI: 10.1299/jcst.3.89]

Young and bulk moduli. To treat such material in an unified way, a mixed finite element method based on the perturbed Lagrange-multiplier method is suitable[5]. Although the displacement finite element method is used with only displacement as the unknown independent variable, the characteristic of the mixed finite element method treats pressure as an unknown independent variable in addition to the displacement. A few studies have been reported using a mixed finite element method for homogenization. Yamamoto et al.[6] showed a formulation in which the compressibility control condition is imposed as a penalty method by eliminating the pressure variables analytically. Heguri et al.[7][8] reported a formulation which applied the Perturbed/Augmented Lagrange-multiplier method to the compressibility control condition, where it is assumed that the existence of a solution with an asymptotic expansion type also applies to the pressure. Recently, to extend the formulation of Heguri et al. to anisotropic material, Matsui et al.[9] attempted a Mixed Finite Element formulation in an infinitesimal deformation problem based on the generalized convergence theory. In the formulations by Heguri and Yamamoto, the pressure in the microstructure is also defined, and an incompressibility condition is given, thus achieving the incompressibility condition of the macroscopic structure. However, the theoretical background and process of numerical realization have not been clear.

The purpose of this study, is to formulate a homogenization method for hyperelastic material using mixed finite element analysis based on two-scale convergence theory[10], while considering the compressibility control and process of numerical realization. As described below, this is achieved using two-scale convergence theory in that the rate of volumetric change of the macrostructure can be controlled by the volume average of the volumetric change of the microstructure corresponding to a point of the macrostructure. From this relationship, the compressibility control condition of the microstructure is considered to be a sufficient condition for the compressibility control of the macrostructure and it is also confirmed under finite element discretization.

2. Nomenclature

$\mathbf{Y}, \mathbf{y}$	:position vectors before and after deformation in the microstructure
$\mathbf{X}, \mathbf{x}$	:position vectors before and after deformation in the macrostructure
$\mathbf{u}$	:macroscopic displacement vector
$\mathbf{w}$	:periodic component of the microscopic displacement vector
$\mathbf{F}$	:the deformation gradient tensor
$\mathbf{Z}$	:the displacement gradient tensor
$\mathbf{E}$	:the Green-Lagrange strain tensor
$\mathbf{\Pi}$	:the first Piola-Kirchhoff stress tensor
$\mathbf{I}$	:the identity tensor
I_c, II_c, III_c	:principal invariants
J	:det $\mathbf{F}$

3. Homogenization Method for the Finite Deformation Problem

3.1. Problem Statement and Geometric Prospect

We assume that the material in the body(Ω) reveals heterogeneity on a very fine scale and is characterized by the periodic distribution of a basic structural element(Y_0) as shown in Fig. 1. The following assumptions of homogenization are employed in the formulation of the homogenization method.

- A macrostructure that consists of a periodic microstructure can be considered to be an approximately equivalent homogeneous substance.
- A microstructure is infinitely fine compared with a macrostructure; the variable defined

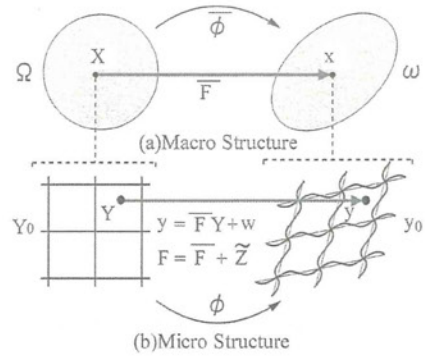

Fig. 1 Homogenization Method in Large Deformation Problem

at each point of the macrostructure corresponds to the volume average of the variables in the microstructure.

To measure the changes in the spatial domains, we introduce two scales: a macro-scale $X \in \Omega$ and a micro-scale $Y \in Y_0$. Thus these scales are characterized by

$$\mathbf{Y} = \mathbf{X}/\epsilon, \tag{1}$$

where ϵ represents the ratio of the two scales. Thus the actual domain can be regarded as the product space $(\Omega \times Y_0)$.

The physical value φ defined in Ω^ϵ is a function dependent on ϵ and is represented by $\varphi^\epsilon(\mathbf{X})$ using ϵ. This can be written as

$$\varphi^\epsilon(\mathbf{X}) = \varphi(\mathbf{X}, \mathbf{X}/\epsilon) = \varphi(\mathbf{X}, \mathbf{Y}) \quad in \quad \Omega \times Y_0, \tag{2}$$

where $\mathbf{X}$ and $\mathbf{Y}$ are independent variables in the micro- and macro-scales, respectively[11]. In the subsequent discussion, a macroscopic quantity defined in Ω corresponding to the microscopic one is expressed by adding a bar symbol over the microscopic symbol.

$\phi : Y_0 \to y_0$ represents the deformation of the microstructure Y_0. This ϕ maps a point $Y \in Y_0$ of the reference configuration onto a corresponding point $y = \phi(Y) \in y_0$ of the current configuration. The associated gradient map of deformation is expressed by $\mathbf{F} = \nabla_Y \mathbf{y}$ and is called the deformation gradient. To indicate components of tensors, we use an orthogonal coordinate system. For instance, $F_{iJ} = y_{i,J} = \partial y_i / \partial Y_J$. The deformation of the microstructure is assumed to be linked to the local values of the macro continuum via

$$\mathbf{y} = \overline{\mathbf{F}}\mathbf{Y} + \mathbf{w}, \tag{3}$$

where $\mathbf{y}$ and $\mathbf{Y}$ are position vectors defined on the microstructure. Briefly, the deformation of the microstructure is assumed to be composed of a homogeneous part $\overline{\mathbf{F}}\mathbf{Y}$, in which $\overline{\mathbf{F}}$ is constant in the microstructure, and a non-homogeneous superimposed periodic field $\mathbf{w}$, usually referred to as the fluctuation field. As illustrated in Fig. 1(b), the deformed thin-line quadrilateral is the homogeneous deformation caused by the macroscopic deformation gradient, and onto it a fluctuation is superimposed. Consequently, the following relationships

$$\mathbf{F} = \nabla_Y \mathbf{y} = \frac{\partial \mathbf{y}}{\partial \mathbf{Y}} = \overline{\mathbf{F}} + \tilde{\mathbf{Z}}, \tag{4}$$

$$\overline{\mathbf{F}} = \nabla_X \mathbf{x} = \frac{\partial \mathbf{x}}{\partial \mathbf{X}}, \tag{5}$$

$$\tilde{\mathbf{Z}} = \nabla_Y \mathbf{w} = \frac{\partial \mathbf{w}}{\partial \mathbf{Y}}. \tag{6}$$

exist between the microscopic and macroscopic deformation gradients. Thus increment and variation of the deformation gradients become

$$\Delta\mathbf{F} = \Delta\overline{\mathbf{F}} + \Delta\tilde{\mathbf{Z}} = \nabla_X \Delta\overline{\mathbf{u}} + \nabla_Y \Delta\mathbf{w} \tag{7}$$

$$\delta\mathbf{F} = \delta\overline{\mathbf{F}} + \delta\tilde{\mathbf{Z}} = \nabla_X \delta\overline{\mathbf{u}} + \nabla_Y \delta\mathbf{w} \tag{8}$$

For the assumptions mentioned above, the macroscopic gradients are related via the volume averages

$$\overline{\mathbf{F}} = \frac{1}{|V|}\int_{Y_0} \mathbf{F}dY = \frac{1}{|V|}\int_{Y_0} (\overline{\mathbf{F}} + \tilde{\mathbf{Z}})dY = \overline{\mathbf{F}} + \frac{1}{|V|}\int_{Y_0} \tilde{\mathbf{Z}}dY, \tag{9}$$

where V is the volume of the microstructure Y_0. Then, the fluctuation field $\mathbf{w}$ has to satisfy the constraint

$$\int_{Y_0} \tilde{\mathbf{Z}}dY = \int_{Y_0} \frac{\partial \mathbf{w}}{\partial \mathbf{Y}}dY = \int_{\partial Y_0} \mathbf{N} \otimes \mathbf{w}dS = \mathbf{0}. \tag{10}$$

Here, $\mathbf{N}$ is an outward normal vector on the boundary ∂Y_0. This constraint is satisfied when $\mathbf{w}$ is periodic.

3.2. Governing Equation

We now consider the equilibrium of material consisting of a periodic microstructure which is modeled by hyperelastic material. Using the principle of stationary potential energy, the equilibrium condition becomes a functional stationary problem. According to the perturbed Lagrange-multiplier method[5], the total potential energy is defined by the functional

$$\Phi_L^\epsilon = \int_{\Omega^\epsilon} W^\epsilon dV^\epsilon + \int_{\Omega^\epsilon} \lambda^\epsilon \left(U^\epsilon - \frac{\lambda^\epsilon}{\kappa}\right) dV^\epsilon + \int_{\partial\Omega^\epsilon} \mathbf{t} \cdot \mathbf{u}^\epsilon dS^\epsilon, \tag{11}$$

where λ is a Lagrange-multiplier corresponding to $-\frac{1}{2}$ of the pressure and which can be considered as two-field variational problems about λ and u. W^ϵ is the energy function for the deviatric elastic response defined by the deviatric part of the deformation gradient ($\mathbf{F}J^{-\frac{1}{3}}$). On the other hand, U^ϵ is the energy function for the volumetric elastic response and is defined by J. $U(J) = 0$, when $J = 1$. κ is the penalty coefficient for volume change control and compressibility can be controlled using this value. The incompressibility condition can be achieved completely as $\kappa \to \infty$. $\mathbf{t}$ is the traction force and we assume a conservative force. The homogenization method for hyperelastic material can thus be reduced to solving the stationary problem of the above functional under the assumption of homogenization. The stationary condition becomes

$$\delta\Phi_L^\epsilon = \int_{\Omega^\epsilon} \left(\delta\mathbf{F}^\epsilon : \mathbf{\Pi}^\epsilon + \delta\lambda^\epsilon \left(U^\epsilon - \frac{2\lambda^\epsilon}{\kappa}\right)\right) dV^\epsilon + \int_{\partial\Omega^\epsilon} \mathbf{t} \cdot \delta\mathbf{u}^\epsilon dS^\epsilon = 0, \tag{12}$$

$$\mathbf{\Pi}^\epsilon = \mathbf{\Pi}_{dev}^\epsilon + \mathbf{\Pi}_{vol}^\epsilon = \frac{\partial W^\epsilon}{\partial \mathbf{F}^\epsilon} + \frac{\partial U^\epsilon}{\partial \mathbf{F}^\epsilon}\lambda^\epsilon. \tag{13}$$

where $\mathbf{\Pi}_{dev}$ is the stress due to the deviatric deformation, and $\mathbf{\Pi}_{vol}$ is the stress due to volume change. To establish the above equation for arbitrary δu^ϵ and $\delta\lambda^\epsilon$, the necessary and sufficient conditions are

$$G_{\delta u^\epsilon} = \int_{\Omega^\epsilon} \delta\mathbf{F}^\epsilon : \mathbf{\Pi}^\epsilon dV^\epsilon + \int_{\partial\Omega^\epsilon} \mathbf{t} \cdot \delta\mathbf{u}^\epsilon dS^\epsilon = 0, \tag{14}$$

$$G_{\delta\lambda^\epsilon} = \int_{\Omega^\epsilon} \delta\lambda^\epsilon \left(U^\epsilon - \frac{2\lambda^\epsilon}{\kappa}\right) dV^\epsilon = 0. \tag{15}$$

Here, Eq. (14) is the equilibrium equation. Because it can also deal with compressible material, Eq. (15) shall be called the compressibility control condition. Thus the pressure p can be described as

$$p^\epsilon = -2\lambda^\epsilon = -\kappa U^\epsilon. \tag{16}$$

3.3. Multi-scale Boundary Value Problem

We adopt the formulation for homogenization based on the two-scale convergence theory proposed by Terada et al.[13].

A sequence of the function $u^\epsilon(\mathbf{X}) \in L^2(\Omega)$ is said to have a two-scale convergence limit $u(\mathbf{X}, \mathbf{Y}) \in L^2(\Omega \times Y_0)$, if for any function $\varphi(\mathbf{X}, \mathbf{Y}) \in D(\Omega; C^\infty_{per}(Y_0))$, we have

$$\lim_{\epsilon \to 0} \int_{\Omega^\epsilon} u^\epsilon(\mathbf{X}) \varphi\left(\mathbf{X}, \frac{\mathbf{X}}{\epsilon}\right) dV^\epsilon = \int_\Omega \frac{1}{|V|} \int_{Y_0} u(\mathbf{X}, \mathbf{Y}) \varphi(\mathbf{X}, \mathbf{Y}) dY dX. \tag{17}$$

where $V = \int_{Y_0} dY$ and $D(\Omega; C^\infty_{per}(Y_0))$ denotes each point $\mathbf{X} \in \Omega$ of the macrostructure corresponding to the smooth and periodic functional space $C^\infty_{per}(Y_0)$, that is, the microstructure. It is also proved that two-scale convergence can be achieved, i.e., the gradient $\nabla_X r^\epsilon(\mathbf{X})$ converges to the combination of the macroscopic and microscopic displacement gradients $\nabla_X \bar{r}(\mathbf{X}) + \nabla_Y r(\mathbf{X}, \mathbf{Y})$[10].

Using the above relationships, Eq. (14) becomes[13]

$$\begin{aligned} G_{\delta u^0} = & \int_\Omega \frac{1}{|V|} \int_{Y_0} (\nabla_X \delta \bar{u}(\mathbf{X}) + \nabla_Y \delta w(\mathbf{X}, \mathbf{Y})) : \mathbf{\Pi}(\mathbf{X}, \mathbf{Y}) dY dX \\ & + \int_{\partial\Omega} \mathbf{t} \cdot \delta \bar{\mathbf{u}}(\mathbf{X}) d\bar{S} = 0 \qquad (18) \\ = & \int_\Omega \frac{1}{|V|} \int_{Y_0} \left(\delta \bar{\mathbf{F}} + \delta \tilde{\mathbf{Z}}\right) : \mathbf{\Pi} dY dX + \bar{G}_{ext} = 0, \qquad (19) \end{aligned}$$

where

$$\bar{G}_{ext}(\delta \bar{\mathbf{u}}) = \int_{\partial\Omega} \mathbf{t} \cdot \delta \bar{\mathbf{u}} d\bar{S}, \tag{20}$$

and Eq. (15) also becomes

$$G_{\delta \lambda^0} = \int_\Omega \frac{1}{|V|} \int_{Y_0} \delta\lambda(\mathbf{X}, \mathbf{Y}) \left(U(\mathbf{X}, \mathbf{Y}) - \frac{2\lambda(\mathbf{X}, \mathbf{Y})}{\kappa}\right) dY dX = 0. \tag{21}$$

Because of the arbitrary nature of variation, the arbitrary function can choose any variation in the admissible functional space. The macroscopic equilibrium equation and compressibility control condition can thus be obtained as

$$G_{\delta \bar{u}} = \int_\Omega \delta \bar{\mathbf{F}}(\mathbf{X}) : \bar{\mathbf{\Pi}} dX - \bar{G}_{ext}(\delta \bar{\mathbf{u}}) = 0, \tag{22}$$

$$\bar{\mathbf{\Pi}} = \frac{1}{|V|} \int_{Y_0} \mathbf{\Pi} dY = \frac{1}{|V|} \int_{Y_0} \left(\frac{\partial W}{\partial \mathbf{F}} + \frac{\partial U}{\partial \mathbf{F}} \lambda\right) dY, \tag{23}$$

$$G_{\delta \bar{\lambda}} = \int_\Omega \delta \bar{\lambda}(\mathbf{X}) \frac{1}{|V|} \int_{Y_0} \left(U - \frac{2\lambda}{\kappa}\right) dY dX = 0, \tag{24}$$

by choosing a variation that only depends on $\mathbf{X}$. In contrast, the following microscopic equilibrium equation and compressibility control condition are obtained

$$G_{\delta u} = \int_{Y_0} \delta \tilde{\mathbf{Z}}(\mathbf{Y}) : \mathbf{\Pi} dY = 0, \tag{25}$$

$$G_{\delta \lambda} = \int_{Y_0} \delta\lambda(\mathbf{Y}) \left(U - \frac{2\lambda}{\kappa}\right) dY = 0, \tag{26}$$

where the volume average of the microscopic volume change determines the macroscopic volume change at an arbitrary point. When Eq. (26) is satisfied for an arbitrary variation $\delta\lambda$,

$$U - \frac{2\lambda}{\kappa} = 0, \tag{27}$$

is satisfied at an arbitrary point in the microstructure. Therefore, if the compressibility control condition is satisfied at a point in the microstructure corresponding to an arbitrary point of the macrostructure, the macroscopic compressibility control condition (Eq. (24)) will automatically be satisfied and this is sufficient using only the microscopic compressibility control condition. This is considered under finite element discretization in the next subsection.

3.4. Finite Element Discretization

We solve Eqs. (22), (25), and (26) using finite element methods. In the hyperelastic material, $\mathbf{\Pi}$ is a function of $\mathbf{F}$ and λ as described above. To solve the nonlinear equation about two variables (u, λ), a Newton-Raphson method is employed. Then, the linearization process of the microscopic equilibrium equation from Eqs. (25) and (26) provides

$$\begin{aligned}\Delta G_{\delta u} &= \int_{Y_0} \delta\tilde{\mathbf{Z}} : \left(\frac{\partial \mathbf{\Pi}}{\partial \overline{\mathbf{F}}} : \Delta\mathbf{F} + \frac{\partial \mathbf{\Pi}}{\partial \lambda}\Delta\lambda\right) dY \\ &= \int_{Y_0} \delta\tilde{\mathbf{Z}} : \left(\mathbf{A} : \Delta\mathbf{F} + \frac{\partial U}{\partial \mathbf{F}}\Delta\lambda\right) dY, \end{aligned} \tag{28}$$

$$\Delta G_{\delta\lambda} = \int_{Y_0} \delta\lambda \left(\frac{\partial U}{\partial \mathbf{F}} : \Delta\mathbf{F} - \frac{2}{\kappa}\Delta\lambda\right) dY, \tag{29}$$

$$\mathbf{A} = \frac{\partial \mathbf{\Pi}}{\partial \mathbf{F}} + \frac{\partial^2 U}{\partial \mathbf{F}\partial \mathbf{F}}\lambda. \tag{30}$$

By using Eq. (7), the linearized microscopic equilibrium equation $G_{\delta u} + \Delta G_{\delta u} = 0$, and the linearized incompressibility condition $G_{\delta\lambda} + \Delta G_{\delta\lambda} = 0$ become

$$\int_{Y_0} \delta\tilde{\mathbf{Z}} : \left(\mathbf{A} : \left(\Delta\overline{\mathbf{F}} + \Delta\tilde{\mathbf{Z}}\right) + \frac{\partial U}{\partial \mathbf{F}}\Delta\lambda\right) dY = -\int_{Y_0} \delta\tilde{\mathbf{Z}} : \mathbf{\Pi} dY, \tag{31}$$

$$\int_{Y_0} \delta\lambda \left(\frac{\partial U}{\partial \mathbf{F}} : \left(\Delta\overline{\mathbf{F}} + \Delta\tilde{\mathbf{Z}}\right) - \frac{2}{\kappa}\Delta\lambda\right) dY = -\int_{Y_0} \delta\lambda \left(U - \frac{2\lambda}{\kappa}\right) dY. \tag{32}$$

Next, we consider the macroscopic equilibrium equation. When Eq. (22) is solved using the Newton-Raphson method, $\overline{G} + \Delta\overline{G} = 0$ becomes

$$\int_\Omega \delta\overline{\mathbf{F}} : \overline{\mathbf{A}} : \Delta\overline{\mathbf{F}} dX = \overline{G}_{ext} - \int_\Omega \delta\overline{\mathbf{F}} : \overline{\mathbf{\Pi}} dX. \tag{33}$$

When the homogenized tangent stiffness is defined as

$$\Delta\overline{\mathbf{\Pi}} = \frac{\partial \overline{\mathbf{\Pi}}}{\partial \overline{\mathbf{F}}} : \Delta\overline{\mathbf{F}} \equiv \overline{\mathbf{A}} : \Delta\overline{\mathbf{F}}, \tag{34}$$

using Eqs. (4) and (23), it becomes

$$\begin{aligned}\overline{\mathbf{A}} &= \frac{\partial \overline{\mathbf{\Pi}}}{\partial \overline{\mathbf{F}}} = \frac{1}{|V|}\int_{Y_0} \frac{\partial \mathbf{\Pi}}{\partial \overline{\mathbf{F}}} dY = \frac{1}{|V|}\int_{Y_0} \left(\frac{\partial \mathbf{\Pi}}{\partial \mathbf{F}} : \frac{\partial \mathbf{F}}{\partial \overline{\mathbf{F}}} + \frac{\partial \mathbf{\Pi}}{\partial \lambda}\frac{\partial \lambda}{\partial \overline{\mathbf{F}}}\right) dY \\ &= \frac{1}{|V|}\int_{Y_0} \left(\mathbf{A} : \frac{\partial(\overline{\mathbf{F}} + \tilde{\mathbf{Z}})}{\partial \overline{\mathbf{F}}} + \frac{\partial U}{\partial \mathbf{F}}\frac{\partial \lambda}{\partial \overline{\mathbf{F}}}\right) dY \\ &= \frac{1}{|V|}\int_{Y_0} \left(\mathbf{A} : \left(\mathbf{I} + \frac{\partial \tilde{\mathbf{Z}}}{\partial \overline{\mathbf{F}}}\right) + \frac{\partial U}{\partial \mathbf{F}}\frac{\partial \lambda}{\partial \overline{\mathbf{F}}}\right) dY. \end{aligned} \tag{35}$$

By inserting Eq. (33) into the above, the linearized macroscopic equilibrium equation is

$$\begin{aligned}&\int_\Omega \delta\overline{\mathbf{F}} : \left(\frac{1}{|V|}\int_{Y_0} \left(\mathbf{A} : \left(\Delta\overline{\mathbf{F}} + \Delta\tilde{\mathbf{Z}}\right) + \frac{\partial U}{\partial \mathbf{F}}\Delta\lambda\right) dY\right) dX \\ &= \overline{G}_{ext} - \int_\Omega \delta\overline{\mathbf{F}} : \left(\frac{1}{|V|}\int_{Y_0} \mathbf{\Pi} dY\right) dX. \end{aligned} \tag{36}$$

Here we use

$$\frac{\partial \tilde{\mathbf{Z}}}{\partial \overline{\mathbf{F}}} : \Delta\overline{\mathbf{F}} = \Delta\tilde{\mathbf{Z}}, \quad \frac{\partial \lambda}{\partial \overline{\mathbf{F}}} : \Delta\overline{\mathbf{F}} = \Delta\lambda. \tag{37}$$

Finally, we obtain three linearized equations, that is, the linearized macroscopic equilibrium equation (31), the linearized microscopic equilibrium equation (32) and the linearized incompressibility condition (36). We now apply a finite element procedure and discretize these equations using

$$\Delta\overline{\mathbf{F}} = [\overline{B}]\Delta\overline{\mathbf{u}}, \tag{38}$$

$$\Delta\tilde{\mathbf{Z}} = [B]\Delta\mathbf{w}, \tag{39}$$

$$\Delta\lambda = \{M\}^T\Delta\Lambda. \tag{40}$$

Then, by multiplying the weight of the macroscopic quadrature point and dividing both sides by $|V|$, the following semi-positive definite symmetric matrix is obtained on the whole macrostructure.

$$\begin{bmatrix} \overline{\mathbf{K}}_{\bar{u}\bar{u}} & \overline{\mathbf{K}}_{\bar{u}w} & \overline{\mathbf{K}}_{\bar{u}p} \\ \mathbf{K}_{w\bar{u}} & \mathbf{K}_{ww} & \mathbf{K}_{wp} \\ \mathbf{K}_{p\bar{u}} & \mathbf{K}_{pw} & \mathbf{K}_{pp} \end{bmatrix} \begin{Bmatrix} \Delta\overline{\mathbf{u}} \\ \Delta\mathbf{w} \\ \Delta\Lambda \end{Bmatrix} = \begin{Bmatrix} \overline{\mathbf{r}}_{\bar{u}} \\ \mathbf{r}_w \\ \mathbf{r}_p \end{Bmatrix}, \tag{41}$$

where

$$\overline{\mathbf{K}}_{\bar{u}\bar{u}} = \int_\Omega [\overline{B}]^T \left(\frac{1}{|V|} \int_{Y_0} [A] dY \right) [\overline{B}] dX \tag{42}$$

$$\overline{\mathbf{K}}_{\bar{u}w} = \int_\Omega [\overline{B}]^T \left(\frac{1}{|V|} \int_{Y_0} [A][B] dY \right) dX \tag{43}$$

$$\overline{\mathbf{K}}_{\bar{u}p} = \int_\Omega [\overline{B}]^T \left(\frac{1}{|V|} \int_{Y_0} \left[\frac{\partial U}{\partial \mathbf{F}} \right] \{M\}^T dY \right) dX \tag{44}$$

$$\mathbf{K}_{w\bar{u}} = \int_\Omega \left(\frac{1}{|V|} \int_{Y_0} [B]^T [A] dY \right) [\overline{B}] dX \tag{45}$$

$$\mathbf{K}_{ww} = \int_\Omega \left(\frac{1}{|V|} \int_{Y_0} [B]^T [A][B] dY \right) dX \tag{46}$$

$$\mathbf{K}_{wp} = \int_\Omega \left(\frac{1}{|V|} \int_{Y_0} [B]^T \left[\frac{\partial U}{\partial \mathbf{F}} \right] \{M\}^T dY \right) dX \tag{47}$$

$$\mathbf{K}_{p\bar{u}} = \int_\Omega \left(\frac{1}{|V|} \int_{Y_0} \{M\} \left[\frac{\partial U}{\partial \mathbf{F}} \right] dY \right) [\overline{B}] dX \tag{48}$$

$$\mathbf{K}_{pw} = \int_\Omega \left(\frac{1}{|V|} \int_{Y_0} \{M\} \left[\frac{\partial U}{\partial \mathbf{F}} \right] [B] dY \right) dX \tag{49}$$

$$\mathbf{K}_{pp} = \int_\Omega \left(\frac{1}{|V|} \int_{Y_0} \{M\} \frac{2}{\kappa} \{M\}^T dY \right) dX \tag{50}$$

$$\overline{\mathbf{r}}_{\bar{u}} = \overline{F}_{ext} - \int_\Omega [\overline{B}]^T \left(\frac{1}{|V|} \int_{Y_0} \{\mathbf{\Pi}\} dY \right) dX \tag{51}$$

$$\mathbf{r}_w = - \int_\Omega \left(\frac{1}{|V|} \int_{Y_0} [B]^T \{\mathbf{\Pi}\} dY \right) dX \tag{52}$$

$$\mathbf{r}_p = - \int_\Omega \left(\frac{1}{|V|} \int_{Y_0} \{M\} \left(U - \frac{2\lambda}{\kappa} \right) dY \right) dX. \tag{53}$$

These are solved about the macroscopic displacement increment $\Delta\mathbf{u}$, the microscopic displacement increment $\Delta\mathbf{w}$, and the Lagrange multiplier increment $\Delta\Lambda$ under the given boundary condition of the macrostructure and periodic boundary condition of the microscopic displacement. If the above equations are statically condensed and both scales are calculated using the weak coupling method as in the study by Miehe et al.[14], a generalized solution using the characteristic deformation χ, including the compressibility control condition, can be obtained.

From Eq. (53), when $\{r_p\}_{ij} = 0$ for component j of all pressure nodes of the microstructure corresponding to the quadrature point i, that is,

$$\{r_p\}_{ij} = \left\{ \frac{1}{|V|} \int_{Y_0} M_j \left(U - \frac{2\lambda}{\kappa} \right) dY \right\}_i = 0, \tag{54}$$

is established, by summing the components of pressure node j,

$$\left\{ \sum_j \frac{1}{|V|} \int_{Y_0} M_j \left(U - \frac{2\lambda}{\kappa} \right) dY \right\}_i = \left\{ \frac{1}{|V|} \int_{Y_0} \sum_j M_j \left(U - \frac{2\lambda}{\kappa} \right) dY \right\}_i = 0. \tag{55}$$

Since $\Sigma_j M_j = 1$ from the nature of the shape function of the finite element method,

$$\left\{ \frac{1}{|V|} \int_{Y_0} \left(U - \frac{2\lambda}{\kappa} \right) dY \right\}_i = 0. \tag{56}$$

The compressibility control condition of the macrostructure, Eq. (24), is also satisfied in a discrete representation at all the quadrature points.

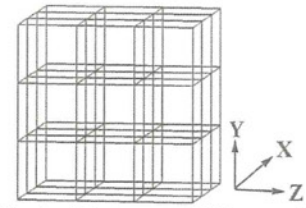

91 nodes (Displacement:64, Pressure:27)
(a)Model 1

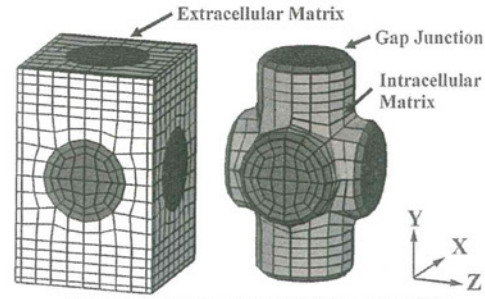

5851 nodes (Displacement:3219, Pressure:2632)
(b) Model 2

Fig. 2 Microscopic FE mesh

4. Numerical Example

For the microstructure, we use the mesh of a block which contains 27 ($3\times3\times3$) elements as shown in Fig. 2(a) as Model 1, and a model simulating cardiomyocyte which is shown in Fig. 2(b) as Model 2. These models are composed of 8/1d elements. Model 2 is an example of the general multiple NDOF (number of degrees of freedom) problem with the distribution of the physical property in the structure. In an element of an 8-node element, there are 8 quadrature points as the macrostructure, and the validity of the proposed method is proved using simple tensile and shear tests. The Mooney-Rivlin material using reduced invariants is assumed for the constitutive equation as

$$W = C_1(\tilde{I}_c - 3) + C_2(\tilde{II}_c - 3), \tag{57}$$

$$\tilde{I}_c = \frac{I_c}{III_c^{1/3}}, \tilde{II}_c = \frac{II_c}{III_c^{2/3}}, \tag{58}$$

$$U = J - 1, \tag{59}$$

where U is the volumetric strain energy function. Then, κ in the above equations becomes the bulk modulus. In addition, when the microstructure includes anisotropic material, it can be described in a similar way by making W a function of IV_c, V_c and so on, that is, Pseudo-Invariants[5].

First, a basic examination is done using Model 1. The material constants of the microstructure are uniform with $C_1 = 1[kPa]$, $C_2 = 1[kPa]$, and $\kappa = 10^4 \times \xi[kPa]$. When a 25[%] uniaxial tensile deformation is given in the y-direction under a nearly incompressible condition ($\xi = 1$), a comparison of the macroscopic and microscopic deformation gradients is given in Table 1 for each of the components. In the case of a uniaxial tensile condition, the deformation gradient is uniform at all the macroscopic quadrature points. Since the material constants of the microstructure are uniform, $\tilde{\mathbf{Z}} = \mathbf{0}$, that is, the deformation gradient at all quadrature points in the microstructure becomes $\overline{\mathbf{F}}$. If this is confined to the case of infinitesimal deformation, Young's modulus E, Poisson's ratio ν, and the shear modulus G of nearly incompressible Mooney-Rivlin material can easily be derived as[16]

$$E = \frac{18(C_1 + C_2)\kappa}{3\kappa + 2(C_1 + C_2)} \tag{60}$$

Table. 1 Deformation gradients for each scale (Model 1)

ij	F_{ij}	$\overline{F}_{ij}$
xx	0.89446810049879	0.89446810049879
xy	0.00000000000000	0.00000000000000
xz	0.00000000000000	0.00000000000000
yx	0.00000000000000	0.00000000000000
yy	1.25000000000000	1.25000000000000
yz	0.00000000000000	0.00000000000000
zx	0.00000000000000	0.00000000000000
zy	0.00000000000000	0.00000000000000
zz	0.89446810049879	0.89446810049879
det**F**	1.00009147851239	1.00009147851239

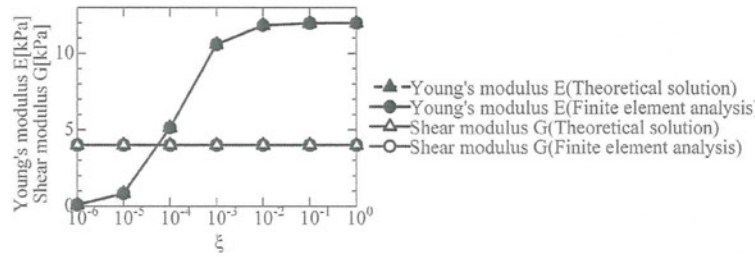

Fig. 3 Homogenized elastic moduli vs. magnitude of bulk modulus (Model 1)

$$\nu = \frac{3\kappa - 4(C_1 + C_2)}{6\kappa + 4(C_1 + C_2)} \tag{61}$$

$$G = 2(C_1 + C_2) \tag{62}$$

which satisfies the relationship of linear elastic material in an infinitesimal deformation

$$\kappa = \frac{E}{3(1-2\nu)}, \quad G = \frac{E}{2(1+\nu)}. \tag{63}$$

In the case of an incompressible condition ($\kappa \to \infty$), $E = 6(C_1 + C_2)$ and ν=0.5, and the shear modulus does not depend on the bulk modulus in an infinitesimal deformation.

Here, if material constants C_1 and C_2 are uniform in the microstructure, the response which is obtained by finite element analysis has to coincide with the theoretical solution Eqs. (60)~(62). The relationship between the homogenized elastic modulus and bulk modulus, which is calculated from macroscopic displacement and loading force is shown in Fig. 3. Young's modulus and the shear modulus agree completely with the theoretical solution. Since the constraint condition is added to all 8 quadrature points of the macrostructure in this analysis, the hardening phenomena occurring due to over-constraint, which is called locking, is anticipated. However, in the incompressible region (near $\kappa = 10^4[kPa]$), no unnatural increase in stiffness is identified. This also agrees with the theoretical solution and thus locking is not observed.

Next we examine Model 2 which simulates the cardiomyocyte. The material constants C_1, C_2 and κ have distributions as given in Table 2. In a uniaxial tensile deformation, the relationship between stretch and volume change of the macrostructure for various bulk moduli of the microstructure using Case 1 parameters is shown in Fig. 4. At $\xi = 1$, a nearly incompressible condition is achieved. Each graph is associated with a different bulk modulus and we can confirm that the magnitude of volume change decreases with a decrease in the bulk modulus of the microstructure. A comparison of the volume change of the microstructure $\left(\frac{1}{|Y|}\int_{Y_0} det\mathbf{F}dY\right)$ and the value of det$\overline{\mathbf{F}}$ at the corresponding macroscopic quadrature point is given in Table 3. We can confirm that both values agree almost completely. This is a result of the prediction from Eqs. (24), (26), (54), and (56). Thus it is clear that the proposed method controls macroscopic volume change using the compressibility condition of the microstructure constraining J(= $det\overline{\mathbf{F}}$) at the macroscopic quadrature point.

Table. 2 Material constants [kPa] (Model 2)

	Case 1			Case 2		
	C_1	C_2	κ	C_1	C_2	κ
Gap Junc.	10	10	$10^5 \times \xi$	1	1	$10^4 \times \xi$
Intra. Matrix	1	1	$10^4 \times \xi$	1	1	$10^4 \times \xi$
Extra. Matrix	0.1	0.1	$10^3 \times \xi$	1	1	$10^4 \times \xi$

Table. 3 Verification of compressibility control condition (Model 2, Case 1)

(a) 10% Tension (Nearly Incompressible $\xi = 1$)

quadrature point	$\frac{1}{\lvert V\rvert}\int_{V_0} \det\mathbf{F}\, dY$	$\det\bar{\mathbf{F}}$
1	1.00002878349178	1.00002878374920
2	1.00002878348170	1.00002878373912
3	1.00002878349414	1.00002878375156
4	1.00002878348402	1.00002878374145
5	1.00002878349418	1.00002878375160
6	1.00002878348403	1.00002878374145
7	1.00002878349654	1.00002878375397
8	1.00002878348636	1.00002878374378
Macroscopic volume change = 1.00002878374904		

(b) 10% Shear (Nearly Incompressible $\xi = 1$)

quadrature point	$\frac{1}{\lvert V\rvert}\int_{V_0} \det\mathbf{F}\, dY$	$\det\bar{\mathbf{F}}$
1	1.00000098498314	1.00000098226455
2	1.00001102789837	1.00001102513974
3	1.00000098461793	1.00000098243829
4	1.00001102799754	1.00001102577960
5	1.00000080584643	1.00000080272925
6	1.00001084609298	1.00001084293560
7	1.00000080548317	1.00000080290299
8	1.00001084619396	1.00001084357545
Macroscopic volume change = 1.00000591347420		

(c) 10% Tension (Compressible $\xi = 10^{-4}$)

quadrature point	$\frac{1}{\lvert V\rvert}\int_{V_0} \det\mathbf{F}\, dY$	$\det\bar{\mathbf{F}}$
1	1.07417781782060	1.07417781839972
2	1.07417780557111	1.07417780615024
3	1.07417781819000	1.07417781876911
4	1.07417780594056	1.07417780651967
5	1.07417781819010	1.07417781876920
6	1.07417780594049	1.07417780651960
7	1.07417781855948	1.07417781913859
8	1.07417780630992	1.07417780688904
Macroscopic volume change = 1.07417781211192		

(d) 10% Shear (Compressible $\xi = 10^{-4}$)

quadrature point	$\frac{1}{\lvert V\rvert}\int_{V_0} \det\mathbf{F}\, dY$	$\det\bar{\mathbf{F}}$
1	1.00674045147491	1.00674044838057
2	1.02716634652040	1.02716634338197
3	1.00674045143295	1.00674044845830
4	1.02716634668573	1.02716634367135
5	1.00668414073269	1.00668413663882
6	1.02710856617705	1.02710856201589
7	1.00668414069160	1.00668413671656
8	1.02710856634320	1.02710856230527
Macroscopic volume change = 1.01692486392233		

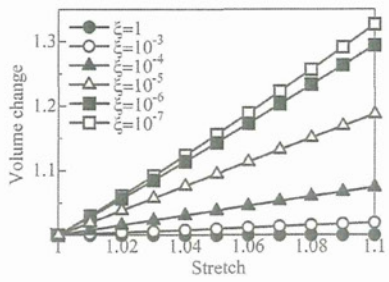

Fig. 4 Volume change in uniaxial tension (Model 2, Case 1)

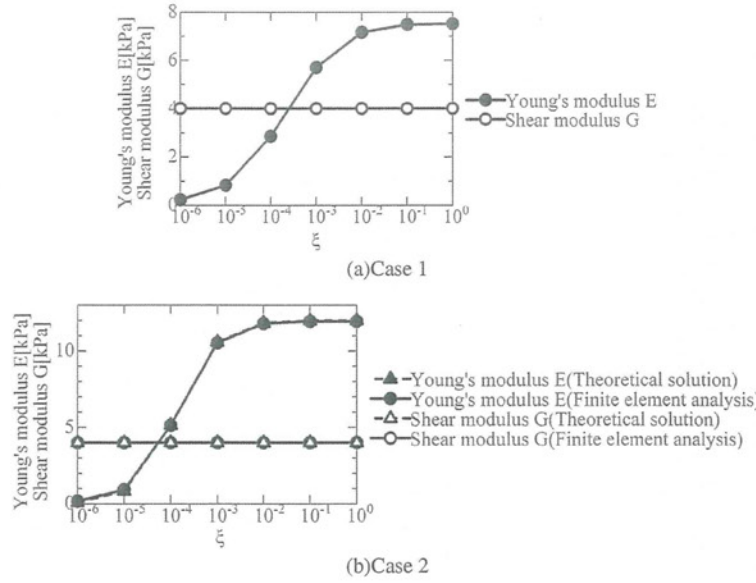

Fig. 5 Homogenized elastic moduli vs magnitude of bulk modulus (Model 2)

Next, we examine uniaxial tensile and simple shear tests in infinitesimal deformation using the parameters in Table 2 for Cases 1 and 2. The relationship between the homogenized elastic modulus and bulk modulus is shown in Fig. 5. Since the values of C_1 and C_2 for the parameters in Case 2 are constant in the microstructure, Young's modulus and the shear modulus obtained in the macrostructure also coincide with the theoretical solution in Eqs. (60)~(62). The graphs for Case 1 show the same trend as for Case 2 and a steep increase in stiffness is not observed as the bulk modulus increases. Young's modulus and the shear modulus in Case 1 are far smaller than in Case 2 reflecting the stiffness distribution of the microstructure. It is thus proved that each macroscopic material property, such as Young's modulus, the bulk modulus, and so on, is determined by the corresponding microscopic material property. No locking is identified in this analysis, and it is thus confirmed that this is a locking free finite element method.

5. Conclusion

The purpose of this paper is to formulate of a homogenization method for hyperelastic material using mixed finite element analysis based on two-scale convergence theory, taking into consideration the compressibility control and process of numerical realization. The proposed method controls macroscopic volume change by constraining J(= $det\overline{\mathbf{F}}$) at the macroscopic quadrature point without the compressibility condition of the macrostructure. The finite element analysis is demonstrated for verification using two different models. The volume change in both the micro and macro structures is compared in both models and the validity of the method is confirmed by comparing these results with the theoretical solution for infinitesimal deformation. In addition, locking of the macrostructure that stems from an incompressible constraint is checked and this method is confirmed to be locking free.

Acknowledgment

This work was supported by a grant from Core Research for Evolutional Science and Technology, Japan Science and Technology Agency. We are deeply grateful to Mr. Washio and Dr. Watanabe in our laboratory who provided insightful comments and suggestions.

References

(1) Terada, K., Hori, M., Kyoya, T. and Kikuchi, N., Simulation of the multi-scale convergence in computational homogenization approaches, *International Journal of Solids and*

Structures, 37 (2000), pp.2285-2311.

(2) Hollister, S.J. and Kikuchi, N., Comparison of homogenization and standard mechanics analyses for periodic porous composites, *Comput. Mech.*, 10 (1992), pp.73-95.

(3) Breuls, R.G.M., Sengers, B.G., Oomens, C.W.J., Bouten, C.V.C. and Baaijens, F.P.T., Predicting Local Cell Deformations in Engineered Tissue Constructs: a Multilevel Finite Element Approach, *ASME J. Biomech. Eng.*, 124(2002), pp.198-207.

(4) Krassowska, W., Pilkington, T.C. and Ideker, R.E., Potential distribution in three-dimensional periodic myocardium: Part I. Solution with two-scale asymptotic analysis, *IEEE Trans. Biomed. Eng.*, 37(1990), pp.252-266.

(5) Holzapfel, G.A., Nonlinear Solid Mechanics: a Continuum Approach for Engineering, John Wiley & Sons, Inc., 2000.

(6) Yamamoto, M. and Hisada, T., A Homogenization Method for Nearly Incompressible Materials by Using Characteristic Deformation Mode Superposition, *Transactions of the Japan Society of Mechanical Engineers Series A*, 45(4) (2002), pp.596-602.

(7) Heguri, H. and Kikuchi, N., Analysis of Incompressible Composites by the Homogenization Method (in Japanese), *Proceedings of the Conference on Computational Engineering and Science*, 3(1998), pp.1007-1010.

(8) Heguri, H. and Kikuchi, N., Analysis of Wavy Fiber Composites by the Nonlinear Homogenization Method (in Japanese), *Proceedings of the Conference on Computational Engineering and Science*, 4(1999), pp.719-722.

(9) Matsui, K. and Yamada, T., The Formulation of Homogenization method by using the Mixed Finite Element Method (in Japanese), *Proceedings of the Conference on Computational Engineering and Science*, 12(2007), pp.301-304.

(10) Allaire, G., Homogenization and two-scale convergence, *SIAM J Math Anal* 23(1992), pp.1482-518.

(11) Terada, K. and Kikuchi, N., Introduction to the method of homogenization (in Japanese), Maruzen, 2003.

(12) Miehe, C., Schroder, J. and Schotte, J., Computational Homogenization Analysis in Finite Plasticity. Simulation of Texture Development in Polycrystalline Materials, *Computer Methods in Applied Mechanics and Engineering*, 171(1999), pp.387-418.

(13) Terada, K., Saiki, I., Matsui, K. and Yamakawa, Y., Two-scale kinematics and linearization for simultaneous two-scale analysis of periodic heterogeneous solids at finite strain, *Computer Methods in Applied Mechanics and Engineering*, 192(2003), pp.3531-3563.

(14) Miehe, C., Schotte, J. and Schroder, J., Computational micro-macro transitions and overall moduli in the analysis of polycrystals at large strains, *Computational Materials Science*, 16(1999), pp.372-382.

(15) Hisada, T. and Noguchi, H., Foundations and Applications of Nonlinear Finite Element Method (in Japanese), Maruzen, 1995.

(16) Watanabe, H., Study of Mixed Finite Element Analysis for Incompressible Hyper-Elastic Materials (in Japanese), Ph.D. Thesis, University of Tokyo, 1995.

Journal of Computational Science and Technology

Vol.3, No.1, 2009

Nonlinear Homogenization Algorithms with Low Computational Cost*

Jun-ichi OKADA**, Takumi WASHIO*** and Toshiaki HISADA†

** Graduate School of Frontier Sciences, University of Tokyo,
5-1-5 Kashiwanoha, Kashiwa, Chiba 277-8563, Japan
E-mail: okada@sml.k.u-tokyo.ac.jp

*** Graduate School of Frontier Sciences, University of Tokyo,
5-1-5 Kashiwanoha, Kashiwa, Chiba 277-8563, Japan
E-mail: washio@sml.k.u-tokyo.ac.jp

† Graduate School of Frontier Sciences, University of Tokyo,
7-3-1 Hongo, Bunkyo-ku, Tokyo 113-0031, Japan
E-mail: hisada@mech.t.u-tokyo.ac.jp

Abstract

An efficient homogenization method for nonlinear problems is introduced. We have already developed a homogenization technique using characteristic deformation mode superposition that avoids prohibitive computational cost. However, in the mode superposition technique, the approximation error created depends on the analysis case. In this paper a new method is proposed, in which the same accuracy as the exact method is preserved by solving the microscopic equilibrium equation, while approximating the tangential matrix of the multi-scale equilibrium equation using the mode superposition method. The performance of the proposed method is examined together with the block LU factorization algorithm, and satisfactory results are obtained.

Key words : Homogenization Method, Nonlinear, Finite Element Analysis, Algorithm, Block LU Factorization, Heart

1. Introduction

The homogenization method is a mathematical modeling technique for efficiently analyzing inhomogeneous material with a periodic microstructure. To measure the spatial change in the domain, we introduce two scales, that is, a scale for the unit period, and a scale for the whole material. By solving the governing equations of both scales with coupling, we can obtain the macroscopic characteristic as an equivalent homogeneous body and variable distribution from the microstructure. To investigate the effect of intracellular structure on heartbeat, we are developing the necessary finite element method which is calculated with the heart as the macrostructure, and the cardiomyocyte as the microstructure.

Biomaterial is usually modeled by hyperelastic material. However, the myofibril in the cardiomyocyte generates contraction forces and stiffness that is changed by chemical reaction and includes high nonlinearity. In the conventional nonlinear homogenization method[(1)(2)], it is necessary to calculate microscopic equilibrium and macroscopic tangential homogenization updates at all quadrature points in every Newton-Raphson iteration, resulting in huge computational cost. To reduce this computational cost, various techniques have been devised. These include, for example, the construction of a database with the homogenized properties[(3)], sensitivity analysis[(4)], Fast Fourier Transforms[(5)], and so on. In a previous paper, to circumvent these difficulties, we proposed the basic framework of a homogenization method that reduces computational cost by using characteristic deformation mode superposition[(6)]. This method is applicable to the microstructure, which is composed of nearly incompressible and viscoelastic materials[(7)(8)]. However, depending on the type of analysis, a significant error may be caused by this technique.

*Received 17 Nov., 2008 (No. T1-07-0747)
Japanese Original: Trans. Jpn. Soc. Mech. Eng., Vol.74, No.738, A (2008), pp.191–200 (Received 20 Aug., 2007)
[DOI: 10.1299/jcst.3.101]